Self-organized cell patterning via mechanical feedback in hindbrain neuropore morphogenesis

Fernanda Pérez-Verdugo,[1] Eirini Maniou,[2,3,4] Gabriel L. Galea,[2,*] and Shiladitya Banerjee[1,*]

[1]*Department of Physics, Carnegie Mellon University, Pittsburgh, PA, USA*
[2]*Developmental Biology and Cancer Department, UCL GOS Institute of Child Health, 30 Guilford Street, London, WC1N 1EH, UK*
[3]*Department of Industrial Engineering, University of Padua, Padua, Italy*
[4]*Veneto Institute of Molecular Medicine, Padua, Italy*

Cell patterning is essential for organized tissue development, enabling precise geometric arrangement of cells, body axis establishment and developmental timing. Here we investigate the role of physical forces and mechanical cues in organizing and maintaining cell morphological patterns during hindbrain neuropore closure, a critical morphogenetic event in vertebrate development. Through live-imaging in mouse embryos and cell-based biophysical modeling, we demonstrate that active cell crawling and actomyosin purse-string contraction at the neuropore border are insufficient to account for the observed cellular arrangements in space and time. Instead, mechanosensitive feedback between cellular stress, shape, and nematic alignment is required to establish and maintain cell morphological patterns and their spatial order. This feedback-driven model generates persistent shape memory in cells, stalls cell rearrangements, and promotes local tissue solidification to preserve the spatial organization during the closure process. We validate this model experimentally, establishing the critical role of mechanical feedback in guiding tissue-level morphogenesis through active, force-driven patterning.

Cell patterning is crucial for embryonic development, establishing the spatial organization of cells and tissues that enables the formation of complex structures and functional organs. This spatial organization is driven by the interplay of physical forces, spatial constraints, and biochemical signals, which collectively guide the emergence of organized, large-scale structures from individual cell behaviors. Here we investigate the mechanisms of cell patterning around the developing neural tube (NT), uncovering how physical forces and tissue mechanics direct spatial arrangements of cells.

NT closure is a critical process in vertebrate development, and failure to close NT gaps, called "neuropores", leads to severe malformations, such as fatal anencephaly [1]. Although previous studies have shown that abnormal tissue mechanics can impede neuropore closure [2–4], the physical mechanisms underlying this process remain poorly understood in mammals. In mice, brain NT closure is completed by closing the hindbrain neuropore (HNP) [5]. The HNP starts as an approximately 700 µm-long gap between the hindbrain/cervical ("Closure 1") and midbrain/hindbrain boundaries ("Closure 2") which closes over 10-12 hours (Fig. **1**A). We previously identified force-generating behaviors of surface ectoderm cells which complete HNP closure [6], showing that coordinated ectodermal cell crawling and supracellular actomyosin purse-string constriction are essential for successful closure. However, how these forces encode cell shape and positional patterns remained unexplored, hindering a bottom-up understanding of HNP morphogenesis.

Using high resolution microscopy of fixed and live-imaged embryos, we now reveal predictable patterns of cell shape and orientation across the surface ectoderm around the HNP. We reveal that cell crawling and purse-string constriction are insufficient to account for cell shape pattering. Rather, mechanosensitive feedback between cell shape, stress and nematic order predicts the emergence and maintenance of cell morphological patterning. Through mechanical feedback, purse-string tension elongates cells along the gap, leading to rostro-caudal elongation along the embryonic midline and stalling cell rearrangements to locally solidify the tissue. We establish an association between cell shape, positional patterns, and tissue solidification that coordinates tissue morphogenesis during HNP closure.

Cell shape patterning and gap morphology during neuropore closure

The HNP gap closure process exhibits robust tissue-level geometric features [6], including the maintenance of an elongated aspect ratio (Fig. **1**A,B and Movie S1), and asymmetric closure dynamics, closing more rapidly from the rostral end compared to the caudal end (Fig. **1**A,C). We found that the cells surrounding the gap (row-1 cells) displayed robust elongation along the gap (Fig. **1**D), producing a predominantly rostro-caudal cellular orientation distribution (Fig. **1**E, blue). Interestingly, this orientation is lost in the next row of cells (Fig. **1**E, red).

We proceeded to quantify metrics of cell geometry, including cell area, aspect ratio, and the cell shape index (perimeter over the square root of the area [7–10]) (Fig. **1**F-H), for the first three cell rows using fixed mouse embryos ranging from the 13 to 17 somite stage. We found that row-1 cells have significantly smaller area than row-2 cells (18% smaller on average, Fig. **1**F). Additionally, we found that the mean cell aspect ratio (Fig. **1**G) and shape index (Fig. **1**H) decrease with the distance away from the gap. Together, these measurements imply that the surface ectoderm maintains a robust patterning of cell morphology around the gap, with highly elongated row-1 cells surrounding the gap and larger row-2 cells.

Cell-based mechanical model of neuropore closure

To uncover the mechanisms regulating cell shape, orientation and collective motion during HNP closure in mouse embryos, we created a vertex-based mechanical model (Fig. **2**A).

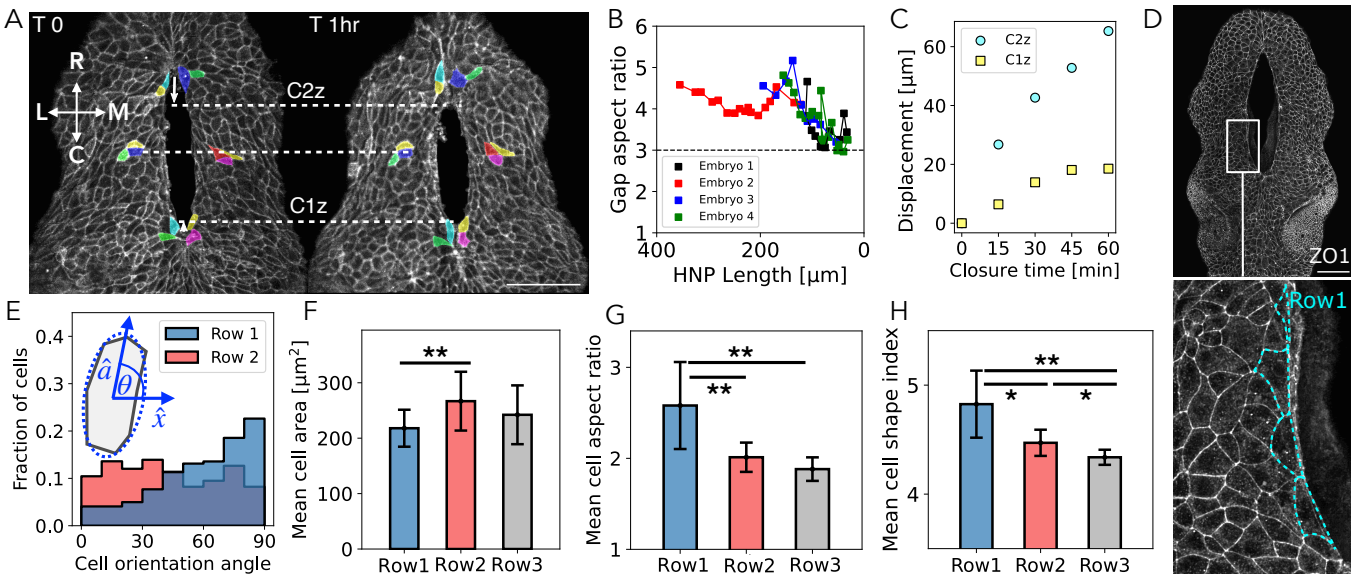

Fig. 1. **Surface ectoderm cells exhibits robust shape patterning during hindbrain neuropore closure.** (A) HNP gap in a 14 somite live-imaged mouse embryo, illustrating the asymmetric closure and the shape evolution of individual cells. C1z and C2z indicate the zippering points progressing from Closure points 1 and 2. Dashed lines indicate landmark positions after 1 hour of live imaging. Colors indicate individual cells. Note cells in contact with C2z at T0 have lost contact with it one hour later whereas cells at C1z remain in contact for the full hour. Scale bar, 100 µm. The solid white arrows indicate the rostro-caudal (R-C) and medio-lateral (M-L) axes. (B) Gap aspect ratio (height over width) versus HNP length, for n=4 live-imaged embryos. Embryos 1-3 (15-16 somite) were previously published [6], and Embryo 4 is shown in (A). (C) Quantification of C2z and C1z (zippering points) displacement over time (from $T = 0$, Fig. 1A). (D) HNP gap in a 15 somite fixed embryo, highlighting the elongation of row-1 surface ectoderm cells (cyan) along the gap. Scale bar, 100 µm. (E-H) Shape analysis of cells in Row 1 (n = 221), Row 2 (n = 316) and Row 3 (n = 376) from 9 embryos. (E) Row-1 and row-2 cellular orientation distributions. The normal vector $\hat{\mathbf{a}}$ defines the cell orientation direction. Cell orientation angle is defined such that $\theta = 90^\circ$ indicates elongation along the rostro-caudal axis. (F) Mean cell area per row. (G) Mean cell aspect ratio per row. (H) Mean cell shape index per row. $*P < 0.05, **P < 0.01$. The analysis shown in (E-H) excludes cells whose centers lie above C2z and below C1z. Error bars represent ± 1 standard deviation.

Specifically, we modeled the squamous surface ectoderm layer as a polygonal cell network in two dimensions, which achieves in-plane deformation to close the HNP. The mechanical energy of the surface ectoderm is given by [7, 11, 12]

$$E = \sum_\alpha \frac{1}{2}\left[K_A\left(A_\alpha - A_0\right)^2 + K_P\left(P_\alpha - P_0\right)^2\right] + \Lambda P_{\text{gap}}\,. \quad (1)$$

The first two terms represent the elastic energy for each cell α, which penalizes changes in cell area A_α and perimeter P_α, with respect to the target values A_0 and P_0. The area and perimeter elastic moduli are given by K_A and K_P, respectively. The third term represents the purse-string mechanical energy, with a high tension Λ along the gap perimeter P_{gap} (red contour in Fig. **2**A,B). We modeled cell migration towards the gap as an active force acting on each vertex i, defined as $\mathbf{F}^i_{\text{crawl}} = \mu v_0 \langle \mathbf{p} \rangle_i$ [13], where μ is the friction coefficient, v_0 is the cell crawling speed, and $\langle \mathbf{p} \rangle_i$ denotes the mean of the cell polarity vector $\mathbf{p}_i$ taken over the neighboring crawling cells. The position $\mathbf{r}_i$ of vertex i evolves in time as:

$$\mu \frac{\mathrm{d}\mathbf{r}_i}{\mathrm{d}t} = -\frac{\partial E}{\partial \mathbf{r}_i} + \mu v_0 \langle \mathbf{p} \rangle_i. \quad (2)$$

Due to the absence of an extracellular matrix ahead of the row-1 cells, it is assumed that row-1 cells cannot actively crawl into the fluid-filled void ahead of them, but assemble nascent matrix underneath as they displace towards the gap [6]. Row-2 cells actively crawl with a unit polarity vector pointing toward the gap. Finally, cells in the third row and beyond act as followers, with their polarity vectors $\mathbf{p}_\alpha$ evolving in time through alignment with their immediate neighbors (denoted by the indices β) as:

$$\frac{\mathrm{d}\mathbf{p}_\alpha}{\mathrm{d}t} = n_{\text{A}} \sum_\beta \left(\mathbf{p}_\beta - \mathbf{p}_\alpha\right) - n_{\text{D}} \mathbf{p}_\alpha, \quad (3)$$

where n_{A} is the polarity alignment rate and n_{D} is the polarity decay rate [14]. These dynamics give rise to a polarity field oriented toward the gap, initiating in the second row of cells, and gradually decaying with distance (Fig. **2**B). This pattern is consistent with our previous visualization of collective displacement of cells in rows 1-3 [6].

Using the model described above, we simulated HNP closure using the parameter values given in Table I (see Supplementary Note 1, Fig. S1 and Movie S2). The model successfully captured the high aspect ratio of the gap throughout the closure process and the asymmetric closure rates, with the rostral zippering point C2z undergoing faster motion compared to the caudal zippering point C1z (Fig. **2**C,D). By varying v_0 and Λ, we found that larger (smaller) values of $\phi = \mu v_0/\Lambda$ led to

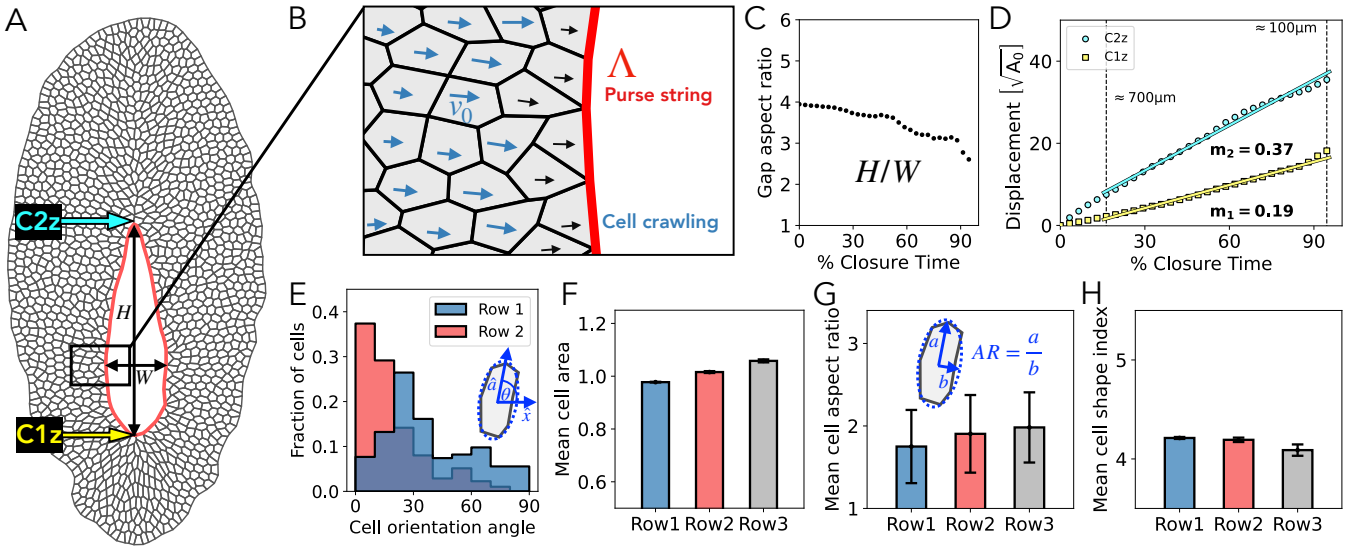

Fig. 2. **Vertex model of neuropore closure via cell crawling and actomyosin contractility does not explain cell shape patterning.** (A) *In silico* tissue snapshot, representing a HNP of height W equal to 400 μm. The shape is evolved from an experimentally-determined starting point, with height $H \sim 850$ μm. C1z (yellow) and C2z (cyan) indicate the zippering points. The red contour highlights the high-tension purse-string along the HNP rim. (B) Schematic of the model for HNP gap closure. Active crawling of row-1 cells is restricted due to the paucity of extracellular matrix in the empty gap ahead of them. Second-row cells actively crawl towards the gap with a speed proportional to v_0, guided by the normal-to-the-gap director of the first-row cells (illustrated by the black arrows). The active crawling speed of subsequent cells diminishes with increasing distance from the gap (illustrated by the length of the blue arrows). (C) HNP gap aspect ratio (H/W) versus percentage closure time. (D) Asymmetric closure of the zippering points C2z and C1z (cyan and yellow arrows in (A)) versus percentage closure time. Vertical black-dashed lines indicates time points at which the system represents a HNP whose height and width are approximately 700 μm and 100 μm, respectively. The solid cyan and yellow lines indicates the linear fit taking the times between the black-dashed lines. The cyan slope (m_2) is approximately twice the yellow slope (m_1). (E) Row-1 and Row-2 cellular orientation. Data account for information during the time window when row-1 consists of $\sim$ 13-36 cells, comparable to the analyses of embryos (Fig. **1**D,F-H). (F-H) Cell shape analysis considering the same time window as in (E). (F) Mean cell area per row. (G) Mean cell aspect ratio per row. (H) Mean cell shape index per row. The cell shape analysis in (E-H) excludes cells whose centers lie above C2z and below C1z. Error bars represent ± 1 standard deviation.

a higher (smaller) gap aspect ratio (see Supplementary Note 1, Fig. S2). Notably, the gap-level features were also achieved when allowing row-1 cells to actively crawl, and in other variants of the model with different rates of polarity alignment and decay (Supplementary Note 1, Fig. S2). This suggests that the gap-level dynamics are highly robust to model variations and depends primarily on the gap geometry.

The vertex model, however, fell short of capturing the patterning of cell shape observed *in vivo*: it did not produce orientation or elongation of cells along the gap (Fig. **2**B,E,G,H and Movie S2). Cell shape index is similar in magnitude across different rows (Fig. **2**H), and much lower than experimentally measured values. Interestingly, the model was able to replicate other statistically significant experimental observations, such as row-2 cells have larger sizes than row-1 cells (Fig.**2**F) and larger perimeters than row-3 cells (Supplementary Note 3, Fig. S3), and cells positioned above C2z are larger than those below C1z (Supplementary Note 3, Fig. S3).

Mechanosensitive feedback underlies cell shape patterning and nematic organization

What causes the observed patterning of cell morphology? Elongation of row-1 cells, oriented along the gap (rostro-caudal axis), can mechanically originate from anisotropic stresses driving cell compression perpendicular to the gap (medio-lateral axis), coupled with extension parallel to the gap. Such anisotropic stresses could arise from actomyosin meshworks generating active contractile or extensile stresses [15–17]. We represent the average orientation of the actin fibers in each cell using the nematic order parameter $\mathbf{Q}_\alpha$ (for cell α), which is a traceless and symmetric tensor that sets the direction of active stress $\mathbf{\Sigma}_\alpha = \Sigma_0 \mathbf{Q}_\alpha$. Here $\Sigma_0 > 0$ is a constant that sets the magnitude of contractile stress that the cell exerts on the surrounding environment. The work done by the anisotropic stress on the surrounding environment depends both on cell shape and nematic order [18], given by $E_{\rm AS} = \frac{1}{2}\sum_\alpha \mathbf{\Sigma}_\alpha : \mathbf{S}_\alpha$, where $\mathbf{S}_\alpha$ is the cell shape tensor (see Supplementary Note 2). This results in an active force exerted by the cells on the surrounding, $\mathbf{F}^i_{\rm AS} = -\partial E_{\rm AS}/\partial \mathbf{r}_i$, where $\mathbf{r}_i$ is the coordinate of the cell vertex i. By Newton's third law, the force on the cell vertex is $-\mathbf{F}^i_{\rm AS}$. As a result, a cell will tend to elongate along the principal axis of $\mathbf{Q}_\alpha$.

This raises the question of how active stress orientation is regulated in the surface ectoderm. Orientational cues may stem from pre-patterned gene expression, chemical signaling, or long-range external stresses resulting from the elongation

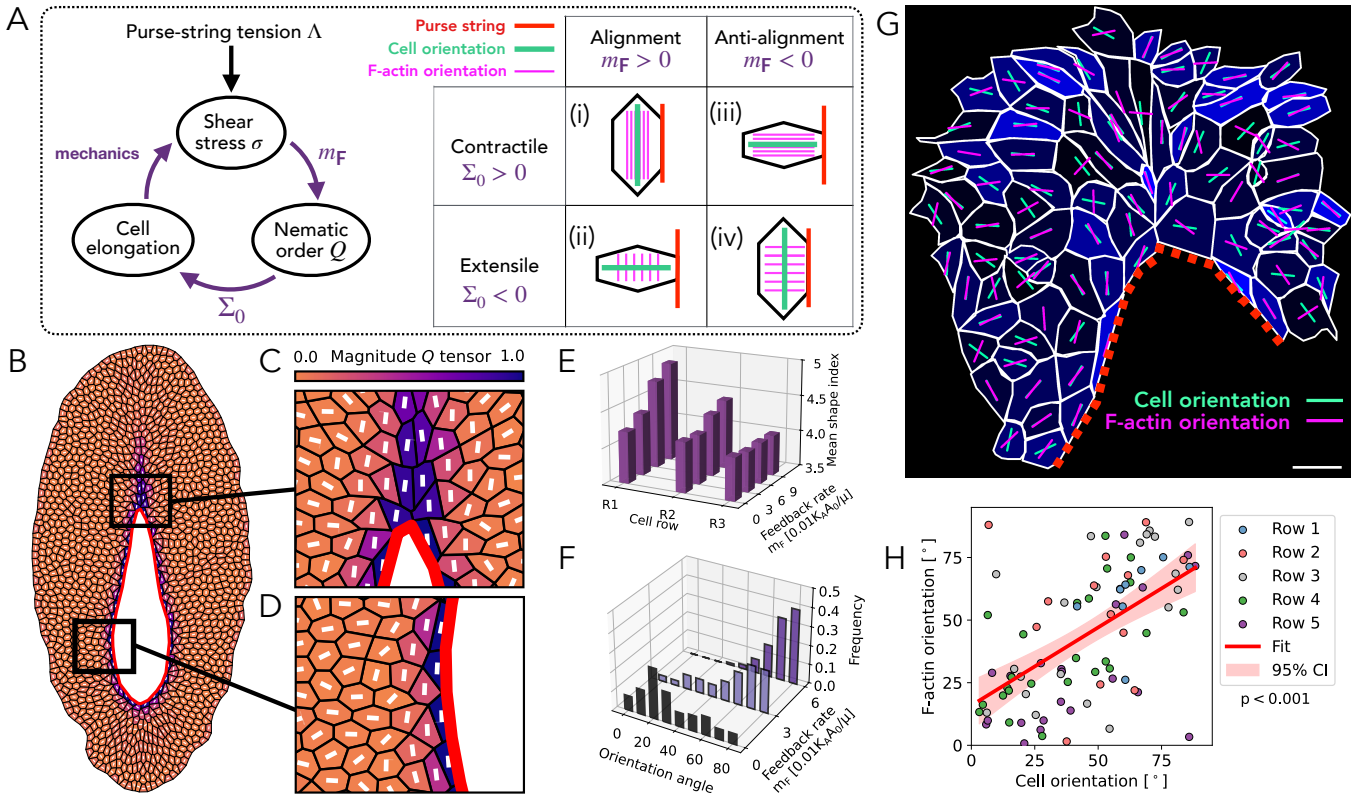

Fig. 3. **Mechanical feedback drives cell shape patterning and nematic organization.** (A) Schematic of the mechanical feedback model between cellular shear stress, nematic order $\mathbf{Q}$, and cell elongation, controlled by the feedback rate m_F and the anisotropic stress magnitude Σ_0. The purse-string tension Λ acts as a mechanical cue to trigger the feedback, driving cell elongation. (i-iv) Different combinations of row-1 cell orientations and nematic organization achieved by the model. (i) Contractile ($\Sigma_0 > 0$) actin filaments aligned ($m_F > 0$) with shear stress; (ii) extensile ($\Sigma_0 < 0$) actin filaments aligned ($m_F > 0$) with shear stress; (iii) contractile ($\Sigma_0 > 0$) actin filaments anti-aligned ($m_F < 0$) with shear stress; and, (iv) extensile ($\Sigma_0 < 0$) actin filaments anti-aligned ($m_F < 0$) with shear stress. (B-D) Application of the model to the HNP gap closure, with $m_F = 0.08$ and $\Sigma_0/K_P = 1$. Tissue snapshot (B), top zoom-in (C), and lateral zoom-in (D) at 50% of closure time. The cell surface color represents the magnitude of the nematic order parameter $\mathbf{Q}$, while the white bars indicate the nematic director. The red contour demarcates the HNP gap boundary. (E-F) Application of the model to the HNP gap closure with varying m_F. (E) Mean cell shape index per row. (F) Row-1 cellular orientation distribution. Cell orientation angle is defined such that $\theta = 90°$ indicates elongation along the rostro-caudal axis. The analysis conducted in panels (E-F) accounts for the time window when row-1 consists of $\sim$ 13-36 cells, comparable to the analyses of embryos and Fig. **1**C,D, and excludes cells above C2z or below C1z. (G) Illustration of surface ectoderm cell shapes and F-actin fibre orientation in cells around the Closure 2 zippering point. White outlines indicate the cell borders, green lines indicate the orientation of each cell's long axis, magenta lines indicate the predominant orientation of their F-actin stress fibers, and blue shading indicates the coherency of their F-actin as defined by OrientationJ. See Supplementary Note 3, Fig. S4 for visualisation of the F-actin fibers. (H) Correlation of surface ectoderm cell long-axis and predominant F-actin stress fiber orientation calculated by OrientationJ (see Methods). Data points represent 88 cells in the embryo shown in Supplementary Note 3,Fig. S4 (representative of 4 equivalently-analyzed embryos).

of the embryo's body axis. In Supplementary Note 4, we discuss how these models fall short in sustaining the elongated cell shapes around the HNP gap during closure. Alternatively, experimental evidence suggests that cells can polarize their actomyosin cytoskeleton in response to mechanical stresses [19–24]. This leads us to propose a mechanosensitive feedback model, in which the purse-string tension serves as a mechanical cue that drives cell shape changes by triggering a feedback between cellular shear stress $\boldsymbol{\sigma}_\alpha$ and nematic order $\mathbf{Q}_\alpha$, such that $\mathbf{Q}_\alpha$ aligns along the direction of maximum shear stress (Fig. **3**A). Specifically, $\mathbf{Q}_\alpha$ is initially null and evolves in time through alignment with neighbors β (with a rate equal to m_A), decay (with a rate equal to m_D), and feedback with shear stress (with a rate equal to m_F):

$$\frac{d\mathbf{Q}_\alpha}{dt} = m_A \sum_\beta (\mathbf{Q}_\beta - \mathbf{Q}_\alpha) - m_D \mathbf{Q}_\alpha + m_F \boldsymbol{\sigma}_\alpha \,, \qquad (4)$$

where all the rate constants are assumed to be positive.

The active force $\mathbf{F}^i_{AS}$ remains unchanged by a simultaneous reversal of the signs of Σ_0 and m_F. For example, when the active stress is extensile ($\Sigma_0 < 0$) and anti-aligns with the shear stress ($m_F < 0$), $\mathbf{F}^i_{AS}$ does not change. However, as we show later, experimental data do not support anti-alignment between nematic order and shear stress. Conversely, if Σ_0 and m_F have opposite signs (Fig.**3**A.ii,iii), $\mathbf{F}^i_{AS}$ promotes cellular

compression along the principal shear axis, inducing elongation perpendicular to the gap, which contradicts experimental observations.

The mechanosensitive feedback model successfully reproduced the elongation of row-1 cells along the gap (Fig. **3**B-D and Movie S3). We considered the limit of high nematic memory, $m_{A,D} \ll m_F$, based on the experimental observation of cells maintaining their elongated shapes (Fig. **1**A). The emergent pattern of the nematic field, representing the principal axis of $\mathbf{\Sigma}_\alpha$, exhibits robust characteristics. First, in close proximity to the gap, lateral regions with low gap curvature exhibit a nematic field parallel to the gap (Fig. **3**B,D), inducing cell elongation along it. Second, once row-1 cells build their anisotropic stress, they are able to retain it for a long time after leaving the gap. This high nematic memory led to a stress field mostly perpendicular to the gap in the region above the zippering point C2z (narrow end, Fig. **3**B,C). In contrast, below the zippering point C1z (wider gap end), the nematic memory induced a transiently oblique nematic field Fig. **3**B. Over time, however, the nematic order parameter gradually aligned with the rostro-caudal axis (see Movie S3).

The model successfully reproduced the observed distribution of cell shape index per row (Fig. **3**E), and the rostro-caudal cell orientation in row-1 (Fig. **3**F) (see Table I for model parameters). Both row-1 cell elongation and rostro-caudal orientation increased with the feedback rate m_F, and the magnitude of the active stress Σ_0 (see Fig. **3**E,F, and Supplementary Note 3, Fig. S5). Additionally, the model predicted a more isotropic cellular orientation distribution in row-2 when increasing m_F and Σ_0, in agreement with the experimental observations (see Fig. **1**E, and Supplementary Note 3, Fig. S6). Importantly, the mechanical feedback led to the expected cell geometrical patterns without interfering with the tissue-level dynamics (see Supplementary Note 3, Fig. S7).

To test the theoretical prediction of actin fiber alignment along the cell's long axis (Fig. **3**B-D), we visualized F-actin distribution using high-resolution wholemount confocal microscopy of the surface ectoderm cells around the HNP in mouse embryos. Each cell has dense F-actin around its apical cell cortex (which largely overlaps with ZO1 staining and was excluded from analysis) and finer filaments resembling stress fibers basally (see Supplementary Note 3, Fig. S4). We quantified the coherence and average orientation of actin fibers and found a robust correlation between cells' long axis and F-actin orientations (Fig. **3**G,H), which becomes particularly evident in cells with high F-actin coherence (see Supplementary Note 3, Fig. S4). These findings are consistent with our model assumption of a contractile nematic stress ($\Sigma_0 > 0$, see Fig. **3**A).

Mechanical feedback explains experimentally-observed midline cell patterns

Our model identifies specific patterns of cell shape that are dependent on the mechanical feedback and can be directly tested with experimental data. Specifically, we found that the row-1 cells leaving the gap formed the midline region in later stages (Fig. **4**A), as seen in embryo live imaging (Fig. **1**A). These midline cells exhibit rostro-caudal elongation (Fig. **4**B). We found consistent results when simulating surface ectoderm midline cells (Fig. **4**C). Additionally, these results are consistent with experimental observations during spinal neural tube closure [3, 25].

We analyzed the morphologies of individual midline cells across 8 fixed embryos with open HNPs. To characterize the shape of these cells, we quantified cell orientation and aspect ratio. We found that the rostral midline cells were oriented along the rostro-caudal axis of the embryo (Fig. **4**D,E), reaching median aspect ratio values of 3.6. Additionally, our analysis of the caudal midline cells also revealed a rostro-caudal orientation, although with significantly lower aspect ratio (~ 2.2) and greater orientation variation (see Supplementary Note 3, Fig. S8). We then performed HNP closure simulations and characterized the shape of midline cells. We found that the predicted rostral midline cell geometry quantitatively agreed with experimental data for sufficiently high anisotropic stress $|\Sigma_0|$ and feedback rate m_F (Fig. **4**D,E). Furthermore, the model with mechanical feedback reproduced the spatial pattern of cell aspect ratio observed in experiments, during and after closure (Fig. **4**F-K). In contrast, a weaker caudal midline cell elongation along with rostro-caudal orientation, emerge independently of the feedback mechanism (see Supplementary Note 3, Fig. S8).

Next we tracked all the prospective midline cells over time, and found that, on average, the mechanical feedback caused their aspect ratios to increase over time, and persist even after gap closure (Fig. **4**L), as corroborated in embryos (see Fig. **4**I). From a side-by-side comparison of cell aspect ratio and instantaneous speed computed from simulations (Fig. **4**G,M), we identified that the midline region is not only characterized by high cell aspect ratio but is also experiencing the largest instantaneous cell speed, with an average value that tends to increase with the feedback rate (Fig. **4**M-O). This underscores the fitness value of cell shape, such that high aspect ratio is associated with faster cell motion.

Mechanical feedback promotes tissue solidity to maintain morphological patterns

The maintenance of cell patterns observable *in vivo* suggests suppression of cell rearrangements which would alter their positions over morphogenetically-relevant timeframes. Cell neighbor exchanges are directly linked to tissue material properties, with fluid tissues exhibiting more exchanges [7, 26]. We thus investigated how tissue material properties are regulated in the surface ectoderm to enable pattern maintenance.

Analysis of our simulations revealed an abundance of 4-fold vertices during HNP closure, mostly positioned around the gap and along the rostro-caudal midline region (Fig. **5**A). These 4-fold vertices represent stalled cell neighbor exchanges that arise during cell intercalations when the resolution of 4-fold vertices into tricellular vertices are energetically unfavorable (see Methods) [26]. Via live imaging we were able to identify the assembly and temporal stability of these structures above the rostral zippering point (Fig. **5**B and

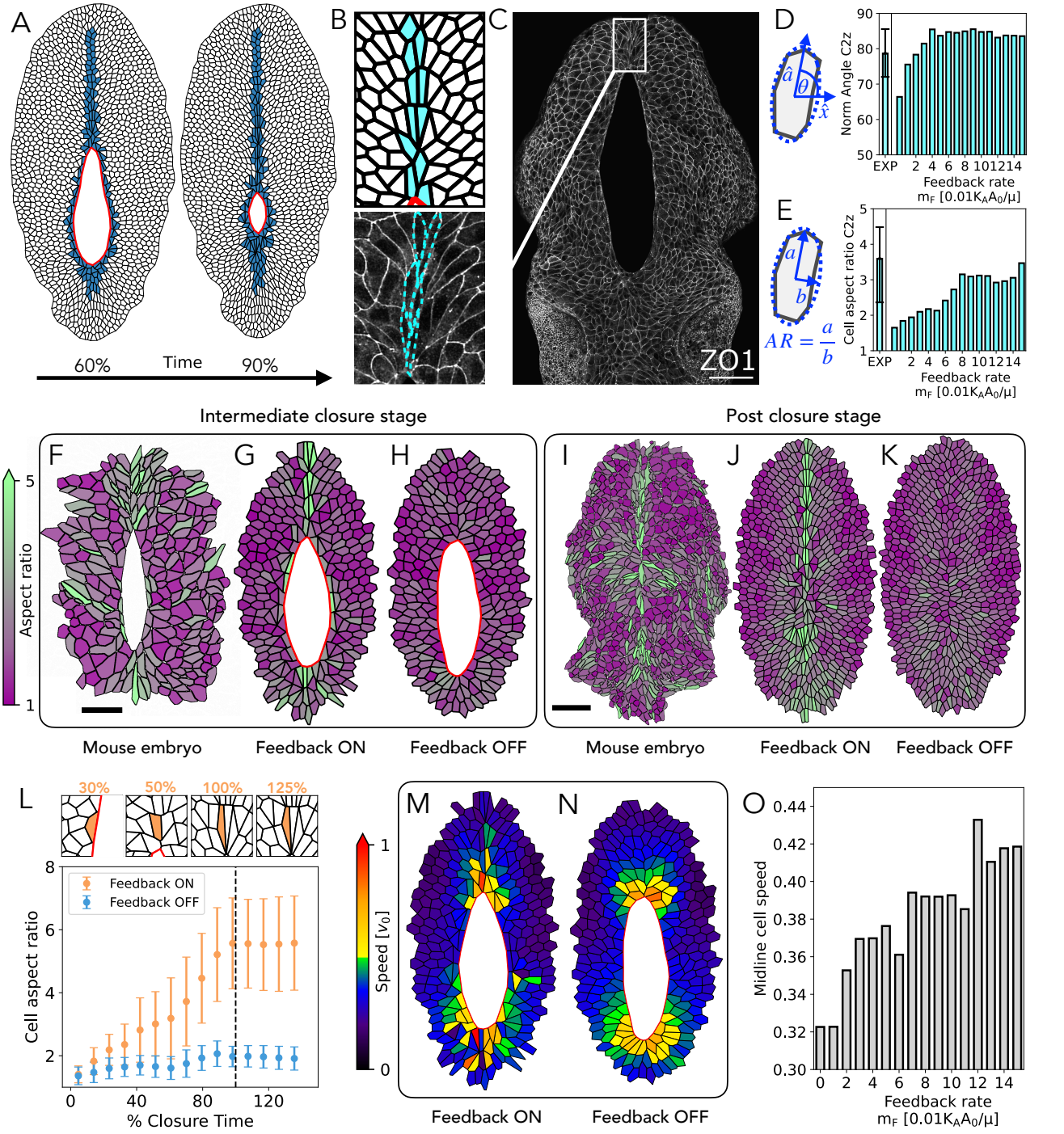

Fig. 4. **Mechanical feedback promotes midline cell elongation and rostro-caudal orientation.** (A) Tissue snapshots using the mechanical feedback model to simulate HNP gap closure with $m_{\mathrm{F}} = 0.08$ and $\Sigma_0/K_P = 1$, at two distinct time points (60% and 90% closure). Blue cells represent the entirety of cells forming row 1 at $t = 0$. (B) Zoomed in snapshot of the midline cells situated just above C2z at 60% closure. Midline region is defined by a rectangle of height equals $10\sqrt{A_0}$ and width equals $1\sqrt{A_0}$, right above the zippering point. (C) HNP gap in a 14 somite fixed embryo, indicating midline cells as in the simulation shown in (B). Scale bar, 100 µm. (D-E) Comparison of rostral midline cell orientation and elongation as a function of the feedback rate m_{F}, between experiments (50 individual cells taken from 8 fixed embryos at 15-17 somite stage), and simulations. Bars denote median value, while the error bars denote the 25/75 percentile range. Simulation data account for information during the time window when row 1 consists of 20 to 50 cells, mirroring experimental conditions. (F-H) Comparison of cell aspect ratio at an intermediate closure stage between a 15 somite mouse embryo (F), and simulations at 80% of closure, with (G) and without (H) the mechanical feedback. Scale bar, 50 µm. (I-K) Comparison of cell aspect ratio at full HNP closure. Scale bar, 100 µm. (L) Zoomed-in midline cell sequence at 4 different times. Comparison of the mean aspect ratio over time for cells that become midline cells (above and below the gap) between 30% and 90% of closure. Error bars represent ±1 standard deviation. (M,N) Comparison of cell speed during HNP closure, with (M) and without (N) feedback. (O) Mean meadline cell (above and below the gap) speed for varying feedback rate.

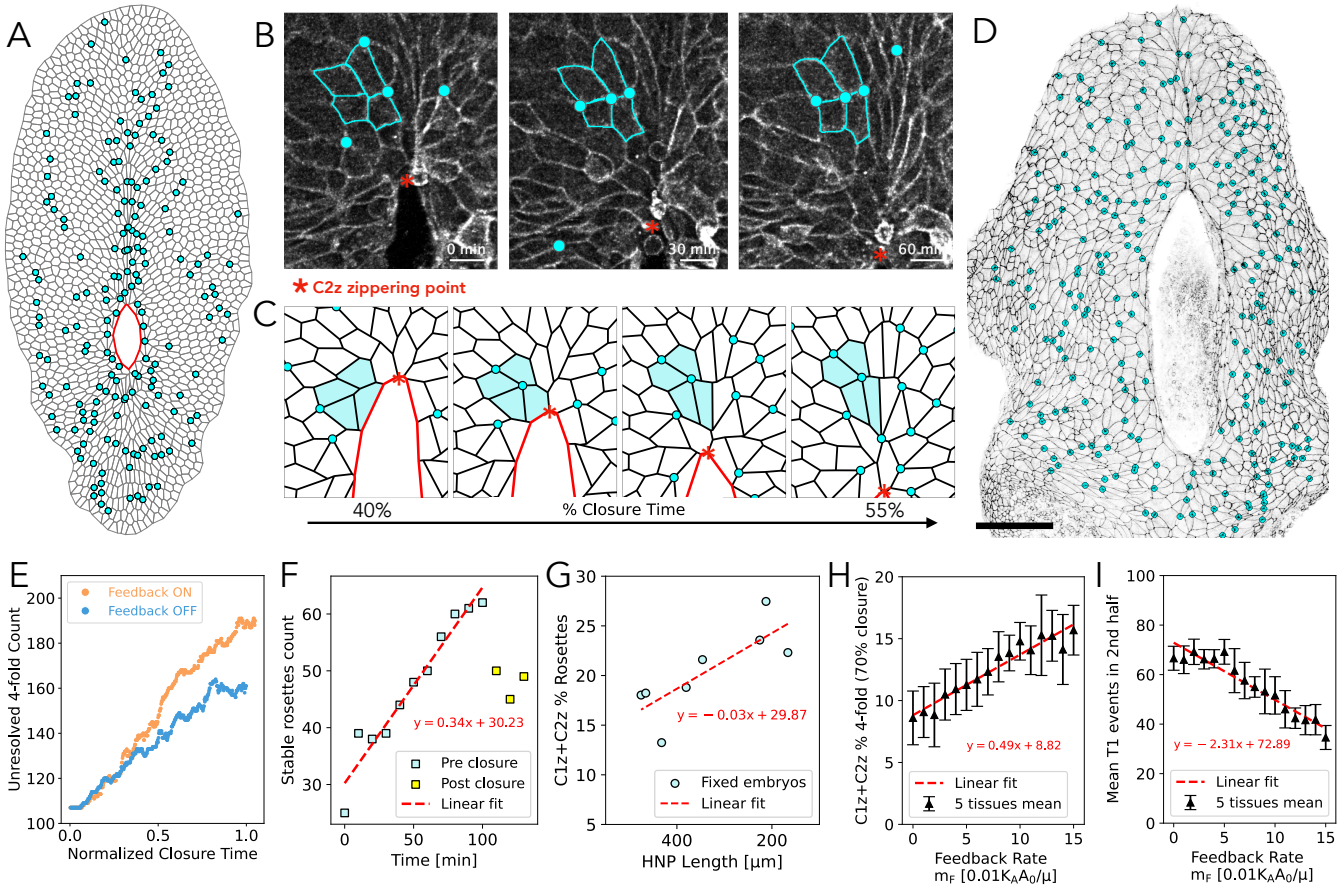

Fig. 5. **Mechanical feedback enhances tissue solidity by stalling T1 transitions.** (A) Tissue snapshot using the mechanical feedback model to simulate HNP gap closure with $m_F = 0.08$ and $\Sigma_0/K_P = 1$, at 90% closure. Cyan dots indicate 4-fold vertices present in the *in silico* surface ectoderm. (B) One-hour live imaging sequence of cells close to C2z, showing the presence of long-lived higher-order vertices (cyan dots). The four cyan cells indicate stable rosettes. Scale bar, 20 μm. (C) Simulation illustrating emergence of a stable 4-fold vertex equivalent to that live-imaging in (B). (D) HNP gap in a fixed embryo, with cyan dots indicating higher-order vertices (4-fold and higher) present in the surface ectoderm. Scale bar, 100 μm. (E) Absolute count of 4-fold vertices present at any given normalized closure time in simulations ($m_F = 0.08$) with and without feedback ($m_F = 0$). (F) Absolute count of stable rosettes over time during live imaging (same as shown in (C)), in a region of size equal to $0.14\,\mathrm{mm}^2$. (G) Fraction of rosettes as a function of HNP length, defined as the number of higher-order cell junctions (≥ 4 cells) over the count of 3-fold vertices, found around C1z and C2z (covering about 225 vertices in each side) in 8 fixed embryos. (H-I) Tissue fluidity characterization in simulations with varying feedback rate. Each data point indicate the mean taken between 5 different simulations (varying initial conditions). (H) Absolute T1 events during the second half of closure. (I) fraction of rosettes at 70% of closure, calculated as in (G), considering circular regions centered at C1z and C2z with a radius equals $7\sqrt{A_0}$.

Movie S4), as predicted by our model (Fig. **5**C and Movie S5). Furthermore, we corroborated the robust presence of higher-order vertices across the surface ectoderm in fixed embryos (Fig. **5**D).

We found that, on average, the number of 4-fold vertices in the simulated tissue increases over time, with a rate that increases with mechanical feedback (Fig. **5**E, S10A,B). We corroborated the increasing presence of stable higher-order vertices ("rosettes") *in vivo* (Fig. **5**F). Furthermore, we analyzed fixed embryos, finding a positive correlation between the fraction of rosettes around the zippering points and closure progression. All these results indicate that the surface ectoderm becomes more solid-like over time, as multicellular rosettes are signatures of tissue solidification [27].

To further characterize the effect of mechanical feedback on tissue solidity, we simulated closure with different initial configurations and quantified the fraction of 4-fold vertices around the zippering points at 70% of gap closure, as well as the absolute number of T1 events. Within our study range, the fraction of 4-fold vertices can increase by up to $\sim 100\%$ (Fig. **5**H), while cell neighbor exchange events can drop by $\sim 50\%$ (Fig. **5**I) for high values of m_F, indicating that tissue solidity is enhanced by the feedback mechanism. Additionally, we found that the HNP closure takes longer with increasing m_F (see Supplementary Note 3, Fig. S10C) - suggesting an evolutionary compromise between cell shape patterning and HNP closure speed.

Outlook

Our work provides evidence that surface ectoderm cells exhibit predictable shape and nematic patterning during mouse HNP closure. We demonstrate that the observed gap dynamics and cell shape patterning can be explained purely by physical arguments. At the tissue-level, dynamics are robustly controlled by directed cell crawling and a purse-string mechanism. However, emergence and maintenance of cell morphological patterning requires active nematic stresses. We show that mechanosensitive feedback between cellular shear stress, nematic alignment, and cell shape can generate spatial patterns observed in experiments. Interestingly, the nematic feedback produces shape "memory" which extends the spatial and temporal outcomes of mechanical cues, in this case from the actomyosin purse-strings limited to the HNP rim. Inference of cellular properties from their shapes should therefore consider their mechanical histories.

The ordered nematic patterning induced by the feedback mechanism leads to localized tissue solidification [9], which, while slowing HNP closure, actively preserves patterning within the surface ectoderm. It is not currently known whether this patterning guides development of derived structures, or is the result of evolutionary constraints imposing the requirement for mechanical feedback. Tissue solidification and deceleration of HNP gap closure is primarily driven by two factors: i) the movement of cells adjacent to the gap, whose dynamics is subject to a rim retraction force generated by anisotropic stress, and ii) the formation of persistent higher-order vertices. Consequently, gap closure times increase as feedback rate increases.

The mechanical feedback mechanisms cannot be neatly identified in embryos with available tools within the short period of HNP closure. Much of the actomyosin machinery is shared between cell types, such that pharmacological modulation dramatically changes tissue geometry [28, 29]. However, it is likely that our findings in the HNP surface ectoderm apply in the spinal region that also produces highly elongated midline cells [3]. Genetic disruption of potential mechanical feedback mechanisms involving myosin recruitment to cell-cell junctions abolishes nematic order of spinal midline cells [3]. In contrast, conditional surface ectoderm deletion of integrin $\beta 1$ produces larger cells which are rostrocaudally oriented with a high aspect ratio[30]. Thus, extrapolation between the cranial and spinal regions suggests that mechanical feedback leading to midline cell elongation may require cell-cell, more than cell-ECM interactions.

Overall, our study highlights crucial roles of mechanics as both a cue and driver of HNP closure. Future work could investigate the molecular mechanisms underpinning this feedback and its generalizability to other biological systems, offering a bottom-up understanding of the physical principles governing epithelial patterning.

Methods

Experimental Methods

Animal Procedures. Studies were performed under the regulation of the UK Animals (Scientific Procedures) Act 1986 and the Medical Research Council's Responsibility in the Use of Animals for Medical Research (1993). C57BL/6J mice were bred in-house and used as plug stock from 8 weeks of age. mTmG mice maintained on a C57BL/6J background were as previously described [31] and tdTom fluorescence from homozygous mTmG embryos was used for live imaging. Mice were time-mated for a few hours during the day and the following midnight was considered E0.5. Pregnant females were sacrificed at E8.5. Embryos with 14-17 somites were analyzed.

Live imaging, immunofluorescence, and image acquisition. Live imaging of tdTom-homozygous embryos was performed as previously described [6, 32]. Whole-mount immunostaining and imaging were also as previously described [2], using rabbit anti-zonula occludens (ZO)1 (Invitrogen 402200, 1:100) primary antibody. Secondary antibodies were used in 1:200 dilution and were Alexa Fluor-conjugated (Thermo Fisher Scientific). Alexa Fluor-647-conjugated Phalloidin was from Thermo Fisher Scientific (A121380). Images were captured on a Zeiss Examiner LSM 880 confocal using 10 x/NA 0.5 or 20 x/NA 1.0 Plan Apochromat dipping objectives and AiryFast. Images were processed with Zen 2.3 software and visualised as maximum projections in ImageJ/Fiji [33]. Linear adjustments were performed equally to all parts of each image. ImageJ/Fiji remove outliers processing was used to eliminate salt and pepper noise for segmentation.

Image analysis. To visualise the surface ectoderm, the z-stacks were first surface-subtracted as previously described [4, 34] to only show the apical 2-5µm of tissue (macro courtesy of Dr. Dale Moulding available at https://github.com/DaleMoulding/Fiji-Macros). Tissue-level morphometric analysis was performed as previously described [6]. Cell morphometric analysis was performed using CellPose segmentation [35] executed in Napari, with manual correction, of ZO1 or phalloidin-stained surfaces. Standard cell shape parameters were measured using in-built functions in ImageJ/Fiji. Heatmap visualizations were created in ImageJ/Fiji, using cell outlines defined in the ROI manager to attribute cell shape properties to their greyscale intensity (scaled from 0-255).

F-actin orientation analysis was performed on surface-subtracted projections using OrientationJ [36–38]. Each cell was manually segmented within the cell cortex (eliminating the cortex from the analysis to avoid the longest cell borders biasing orientation quantification). F-actin filament staining intensity was equalized using the contrast-limited adaptive histogram enhancer (CLAHE) plugin (bin size = 50, histogram = 200, slope 3, slow processing) to account for variation in apparent intensity following surface-subtraction.

Surface projection was achieved using a previously-reported analysis pipeline [34] in which the top-most surface

of the tissue is identified and a specified thicknesses of signal projected, excluding signal from cells below the surface ectoderm. Images were captured on a Zeiss LSM880 microscope with a 20x objective NA1 using AiryFast Super Resolution. Cell long axis orientation was calculated using the *fit ellipse* function in Fiji. F-actin orientation was calculated in individual cells using the plug-in OrientationJ [38], available online at https://bigwww.epfl.ch/demo/orientation/. F-actin stress fibres were accentuated before orientation analysis using the CLAHE function in Fiji (block size 50, bins 100, slope 3).

Statistical Analysis. The statistical analysis shown in Fig. **1**F-H considers individual embryos as the unit of measure, and was performed in Excel 16.72. The rest of the statistical analysis considers individual cells as the unit of measure, and was performed in Python 3.9.7 (numpy 1.20.3). Comparison of two groups was by Student's t-test, paired by embryo where appropriate. Graphs were made in Python 3.9.7 (matplotlib 3.4.3) and are shown either as bar plots or as scatter plots. For bar plots, the bar shows the mean or median value, depending on the figure and described in each caption. The error bars indicate ± 1 standard deviation or the 25/75 percentile range, depending on the figure and described in each caption.

Computational Methods

Vertex Model Initialization. On average, the HNP forms at the 12-somite stage, exhibiting an asymmetric and elongated gap that is narrower at the rostral extreme (drop-like shape). The gap height and width reach up to 600 µm and 150 µm, respectively [6]. The closure of the HNP is typically completed by the 17-somite stage, taking 10 to 12 h. The typical cell area at early stages is $\sim 200\,\mu\text{m}^2$. To simulate HNP closure, we use an active vertex model where each cell is represented by a polygon whose vertices move in time following an overdamped equation of motion subjected to the forces of friction, tension, elasticity, and active crawling. We nondimensionalized the equations using $K_A A_0^{3/2}$ as the force scale, $\sqrt{A_0}(\approx 14\,\mu\text{m})$ as the length scale, $\mu/K_A A_0$ as the time scale, and set $A_0 = 1$, $K_A = 1$, and $\mu = 1$.

The morphological cell patterning with row-1 cells exhibiting elongation along the gap is already observed at the 12-somite stage. Since in this work we aim at explaining the origin and maintenance of cell heterogeneity, we created an initial configuration that represent an earlier stage. Specifically, we generated a free (outer) boundary condition disordered tissue, composed of 1427 cells, with a gap that has a height equals $H \sim 60\sqrt{A_0} \approx 850\,\mu\text{m}$, and a width equals $W \sim 15\sqrt{A_0} \approx 210\,\mu\text{m}$.

Numerical integration. The differential equations are integrated using the Euler integration method, with a time step fixed to $\Delta t = 0.05$.

Rules for T1 transitions. When a cell-cell junction connected by two 3-fold vertices becomes shorter than a threshold length $l_{T_1} = 0.05$, one of the vertices is removed, and the other is transformed into a 4-fold vertex, sustained by four shoulder junctions. At each time step, we attempt 4-fold vertex resolution in both the original (reversible T1-transition) and perpendicular (T1-transition) directions. The resolution is allowed only when the new configuration pushes the new 3-fold vertices apart in the direction of the largest repulsive force [26]. For the resolution attempts, we particularly consider the forces arising from elasticity and anisotropic stresses (both associated with energy terms), as well as the active crawling forces. Since the polarity field decays smoothly in the bulk region with cell-cell junctions, stalled 4-fold vertices indicate energetically unfavorable T1-transitions.

If a cell-void junction becomes shorter than a threshold length $l_{T_1} = 0.05$, a T1-transition is performed instantaneously. Note that in this case, the junction is initially connected by two 2-fold vertices, whereas after the T1-transition, one of those vertices becomes a 3-fold.

Feedback Model. Our feedback model considers that cells are able to sense the local shear stress σ, and adjust the orientation of actin fibers in response. Here, we compute the tensor σ for a given cell α following the formalism previously described in Ref. [39],

$$\sigma^{\alpha}_{mn} = \frac{1}{A_\alpha} \sum_{\langle i,j\rangle_\alpha} \frac{[K_P\,(P_\alpha - P_0) + T_{ij}]}{|\mathbf{r}_i - \mathbf{r}_j|} \left[s^{(i,j)}_{mn} - \frac{1}{2}\text{Tr}s^{(i,j)}\delta_{mn} \right], \tag{5}$$

where the sum runs over adjacent vertices i, j belonging to the cell α, with positions $\mathbf{r}_i$ and $\mathbf{r}_j$, respectively, and $s^{(i,j)} = (\mathbf{r}_i - \mathbf{r}_j) \otimes (\mathbf{r}_i - \mathbf{r}_j)$. The variable T_{ij} can take the value $T_{ij} = \Lambda$ if the junction is part of the gap boundary, $T_{ij} = \Lambda_{\text{out}}$ if the junction is part of the outer boundary, or $T_{ij} = 0$, the junction is in the bulk. We neglect stresses arising from active crawling [40, 41] in our mechanical feedback.

The nematic orientation of F-actin within a cell α, $\mathbf{Q}_\alpha$, leads to an anisotropic cellular stress given by $\mathbf{\Sigma}_\alpha = \Sigma_0 \mathbf{Q}_\alpha$. Σ_0 is a constant that sets the magnitude of the maximum contractile stress the cell exert over the substrate, and $\mathbf{Q}_\alpha$ is a two-dimensional nematic tensor (traceless and symmetric tensor), defined by the magnitude $Q_{0\alpha}/2$ and the principal nematic director $\hat{\mathbf{n}}^q$. Then, the work performed by the anisotropic stress on the surrounding environment is given by $E_{\text{AS}} = \frac{1}{2}\sum_\alpha \mathbf{\Sigma}_\alpha : \mathbf{S}_\alpha$ [18], where $\mathbf{A} : \mathbf{B} = A_{ij}B_{ij} = \text{Tr}\left(AB^T\right)$ (full tensor contraction), and $\mathbf{S}_\alpha$ is the shape cell tensor given by $\mathbf{S}_\alpha = \sum_{\langle i,j\rangle_\alpha} {l_{ij}}^2\,(\hat{\mathbf{n}}_{ij} \otimes \hat{\mathbf{n}}_{ij})$, where $\mathbf{l}_{ij} = \mathbf{r}_i - \mathbf{r}_j$, $l_{ij} = |\mathbf{l}_{ij}|$, and $\hat{\mathbf{n}}_{ij} = \mathbf{l}_{ij}/l_{ij}$. Then, the work can be written as the following:

$$E_{\text{AS}} = \frac{1}{2}\Sigma_0 \sum_\alpha \sum_{\langle i,j\rangle_\alpha} Q_{0\alpha} l_{ij}^2 \left[\left(\hat{\mathbf{n}}^q_\alpha \otimes \hat{\mathbf{n}}^q_\alpha - \frac{1}{2}\mathbb{I} \right) : (\hat{\mathbf{n}}_{ij} \otimes \hat{\mathbf{n}}_{ij}) \right], \tag{6}$$

where $\mathbb{I}$ the two-dimensional identity matrix. By writing the previous tensors in the basis $\{\hat{\mathbf{n}}^q_\alpha, \hat{\mathbf{m}}^q_\alpha\}$, with $\hat{\mathbf{m}}^q_\alpha = \hat{\mathbf{z}} \times \hat{\mathbf{n}}^q_c$, we obtain the following form for the energy cost:

$$E_{\rm AS} = \frac{1}{2}\Sigma_0 \sum_{\alpha} \sum_{\langle i,j\rangle_\alpha} |\,\mathbf{Q}_\alpha| \left(\left[\mathbf{l}_{ij}\cdot\hat{\mathbf{n}}_\alpha^q\right]^2 - \left[\mathbf{l}_{ij}\cdot\hat{\mathbf{m}}_\alpha^q\right]^2 \right), \qquad (7)$$

where the first sum is over the α cells to which the vertex i belongs to, and the second sum runs over the j adjacent vertices, belonging to the cell α. From the last quadratic-length form it is clear that the surrounding material will tend to elongate in the axis defined by $\hat{\mathbf{m}}_c^q$ (extensile direction), with a magnitude of the stress given by $\Sigma_0|\mathbf{Q}_\alpha| = \Sigma_0 Q_{0\alpha}/2$. Finally, each vertex i defining the cell boundary is subject to an extra force given by $-\mathbf{F}^i_{\rm AS} = \partial E_{\rm AS}/\partial \mathbf{r}_i$.

Default model parameter	Symbol	Value
Area elastic modulus	K_A	1
Mean preferred area	A_0	1
Mean preferred perimeter	P_0	3.5
Friction coefficient	μ	1
Gap tension	Λ	0.1
Outer tension	$\Lambda_{\rm out}$	0.01
Perimeter contractility	K_P	0.01
Length threshold for T1 transitions	l_{T_1}	0.05
Crawling speed	v_0	0.04
Crawling polarity alignment rate	$n_{\rm A}$	0.01
Crawling polarity decay rate	$n_{\rm D}$	0.01
Integration time step	Δt	0.05
Feedback model parameter	**Symbol**	**Value**
Anisotropic stress amplitude	Σ_0	0,-0.01
Anisotropic stress alignment rate	$m_{\rm A}$	0.001
Anisotropic stress decay rate	$m_{\rm D}$	0.001
Mechanical feedback rate	$m_{\rm F}$	0-0.15

TABLE I. Default model parameters.

Acknowledgements

SB acknowledges support from the National Institutes of Health (NIH R35 GM143042) and the National Science Foundation (NSF MCB-2203601). GLG acknowledges support from the Wellcome Trust (211112/Z/18/Z), Royal Society (RG\R2\232082) and Leverhulme Trust (RPG-2024-147). EM acknowledges support from European Union's Horizon 2021 Marie Sklodowska-Curie grant agreement no. 101067028. The surface subtraction macro is courtesy of Dr. Dale Moulding and available on GitHub (https://github.com/DaleMoulding/Fiji-Macros).

* Correspondence: shiladtb@andrew.cmu.edu or g.galea@ucl.ac.uk

[1] E. Nikolopoulou, G. L. Galea, A. Rolo, N. D. Greene, and A. J. Copp, Neural tube closure: cellular, molecular and biomechanical mechanisms, Development **144**, 552 (2017).

[2] G. L. Galea, Y.-J. Cho, G. Galea, M. A. Molè, A. Rolo, D. Savery, D. Moulding, L. H. Culshaw, E. Nikolopoulou, N. D. Greene, *et al.*, Biomechanical coupling facilitates spinal neural tube closure in mouse embryos, Proceedings of the National Academy of Sciences **114**, E5177 (2017).

[3] E. Nikolopoulou, C. S. Hirst, G. Galea, C. Venturini, D. Moulding, A. R. Marshall, A. Rolo, S. C. De Castro, A. J. Copp, and N. D. Greene, Spinal neural tube closure depends on regulation of surface ectoderm identity and biomechanics by grhl2, Nature communications **10**, 2487 (2019).

[4] G. L. Galea, E. Maniou, T. J. Edwards, A. R. Marshall, I. Ampartzidis, N. D. Greene, and A. J. Copp, Cell non-autonomy amplifies disruption of neurulation by mosaic vangl2 deletion in mice, Nature communications **12**, 1159 (2021).

[5] A. J. Copp, N. D. Greene, and J. N. Murdoch, The genetic basis of mammalian neurulation, Nature Reviews Genetics **4**, 784 (2003).

[6] E. Maniou, M. F. Staddon, A. R. Marshall, N. D. Greene, A. J. Copp, S. Banerjee, and G. L. Galea, Hindbrain neuropore tissue geometry determines asymmetric cell-mediated closure dynamics in mouse embryos, Proceedings of the National Academy of Sciences **118**, e2023163118 (2021).

[7] D. Bi, J. Lopez, J. M. Schwarz, and M. L. Manning, A density-independent rigidity transition in biological tissues, Nature Physics **11**, 1074 (2015).

[8] J.-A. Park, J. H. Kim, D. Bi, J. A. Mitchel, N. T. Qazvini, K. Tantisira, C. Y. Park, M. McGill, S.-H. Kim, B. Gweon, *et al.*, Unjamming and cell shape in the asthmatic airway epithelium, Nature materials **14**, 1040 (2015).

[9] X. Wang, M. Merkel, L. B. Sutter, G. Erdemci-Tandogan, M. L. Manning, and K. E. Kasza, Anisotropy links cell shapes to tissue flow during convergent extension, Proceedings of the National Academy of Sciences **117**, 13541 (2020).

[10] S. Grosser, J. Lippoldt, L. Oswald, M. Merkel, D. M. Sussman, F. Renner, P. Gottheil, E. W. Morawetz, T. Fuhs, X. Xie, *et al.*, Cell and nucleus shape as an indicator of tissue fluidity in carcinoma, Physical Review X **11**, 011033 (2021).

[11] T. Nagai and H. Honda, A dynamic cell model for the formation of epithelial tissues, Philosophical Magazine B **81**, 699 (2001).

[12] R. Farhadifar, J.-C. Röper, B. Aigouy, S. Eaton, and F. Jülicher, A dynamic cell model for the formation of epithelial tissues, Current biology **17**, 2095 (2007).

[13] M. F. Staddon, D. Bi, A. P. Tabatabai, V. Ajeti, M. P. Murrell, and S. Banerjee, Cooperation of dual modes of cell motility promotes epithelial stress relaxation to accelerate wound healing, PLoS computational biology **14**, e1006502 (2018).

[14] M. F. Staddon, M. P. Murrell, and S. Banerjee, Interplay between substrate rigidity and tissue fluidity regulates cell monolayer spreading, Soft Matter **18**, 7877 (2022).

[15] S. Stam, S. L. Freedman, S. Banerjee, K. L. Weirich, A. R. Dinner, and M. L. Gardel, Filament rigidity and connectivity tune the deformation modes of active biopolymer networks, Proceedings of the National Academy of Sciences **114**, E10037 (2017).

[16] J. Berezney, B. L. Goode, S. Fraden, and Z. Dogic, Extensile to contractile transition in active microtubule–actin composites generates layered asters with programmable lifetimes, Proceedings of the National Academy of Sciences **119**, e2115895119 (2022).

[17] M. Lenz, Reversal of contractility as a signature of self-organization in cytoskeletal bundles, Elife **9**, e51751 (2020).

[18] C. Duclut, J. Paijmans, M. M. Inamdar, C. D. Modes, and F. Jülicher, Active t1 transitions in cellular networks, The European Physical Journal E **45**, 1 (2022).

[19] B. Ladoux, R.-M. Mège, and X. Trepat, Front–rear polarization by mechanical cues: from single cells to tissues, Trends in Cell

Biology **26**, 420 (2016).

[20] K. Ohashi, S. Fujiwara, and K. Mizuno, Roles of the cytoskeleton, cell adhesion and rho signalling in mechanosensing and mechanotransduction, The journal of biochemistry **161**, 245 (2017).

[21] S. Majumdar, L. C. Foucard, A. J. Levine, and M. L. Gardel, Mechanical hysteresis in actin networks, Soft Matter **14**, 2052 (2018).

[22] M. Duda, N. J. Kirkland, N. Khalilgharibi, M. Tozluoglu, A. C. Yuen, N. Carpi, A. Bove, M. Piel, G. Charras, B. Baum, *et al.*, Polarization of myosin ii refines tissue material properties to buffer mechanical stress, Developmental Cell **48**, 245 (2019).

[23] N. Khalilgharibi, J. Fouchard, N. Asadipour, R. Barrientos, M. Duda, A. Bonfanti, A. Yonis, A. Harris, P. Mosaffa, Y. Fujita, *et al.*, Stress relaxation in epithelial monolayers is controlled by the actomyosin cortex, Nature Physics **15**, 839 (2019).

[24] N. A. Dye, M. Popović, K. V. Iyer, J. F. Fuhrmann, R. Piscitello-Gómez, S. Eaton, and F. Jülicher, Self-organized patterning of cell morphology via mechanosensitive feedback, Elife **10**, e57964 (2021).

[25] A. R. Marshall, G. L. Galea, A. J. Copp, and N. D. Greene, The surface ectoderm exhibits spatially heterogenous tension that correlates with yap localisation during spinal neural tube closure in mouse embryos, Cells & Development **174**, 203840 (2023).

[26] F. Pérez-Verdugo and S. Banerjee, Tension remodeling regulates topological transitions in epithelial tissues, PRX Life **1**, 023006 (2023).

[27] L. Yan and D. Bi, Multicellular rosettes drive fluid-solid transition in epithelial tissues, Physical Review X **9**, 011029 (2019).

[28] P. Ybot-Gonzalez and A. J. Copp, Bending of the neural plate during mouse spinal neurulation is independent of actin microfilaments, Developmental dynamics: an official publication of the American Association of Anatomists **215**, 273 (1999).

[29] S. Escuin, B. Vernay, D. Savery, C. B. Gurniak, W. Witke, N. D. Greene, and A. J. Copp, Rho-kinase-dependent actin turnover and actomyosin disassembly are necessary for mouse spinal neural tube closure, Journal of cell science **128**, 2468 (2015).

[30] M. A. Mole, G. L. Galea, A. Rolo, A. Weberling, O. Nychyk, S. C. De Castro, D. Savery, R. Fässler, P. Ybot-Gonzalez, N. D. Greene, *et al.*, Integrin-mediated focal anchorage drives epithelial zippering during mouse neural tube closure, Developmental Cell **52**, 321 (2020).

[31] M. D. Muzumdar, B. Tasic, K. Miyamichi, L. Li, and L. Luo, A global double-fluorescent cre reporter mouse, genesis **45**, 593 (2007).

[32] M. A. Molè, G. L. Galea, and A. J. Copp, Live-imaging analysis of epithelial zippering during mouse neural tube closure, in *Cell Migration in Three Dimensions*, edited by C. Margadant (Springer US, New York, NY, 2023) pp. 147–162.

[33] J. Schindelin, I. Arganda-Carreras, E. Frise, V. Kaynig, M. Longair, T. Pietzsch, S. Preibisch, C. Rueden, S. Saalfeld, B. Schmid, *et al.*, Fiji: an open-source platform for biological-image analysis, Nature methods **9**, 676 (2012).

[34] G. L. Galea, O. Nychyk, M. A. Mole, D. Moulding, D. Savery, E. Nikolopoulou, D. J. Henderson, N. D. Greene, and A. J. Copp, Vangl2 disruption alters the biomechanics of late spinal neurulation leading to spina bifida in mouse embryos, Disease models & mechanisms **11**, dmm032219 (2018).

[35] C. Stringer, T. Wang, M. Michaelos, and M. Pachitariu, Cellpose: a generalist algorithm for cellular segmentation, Nature methods **18**, 100 (2021).

[36] Z. Püspöki, M. Storath, D. Sage, and M. Unser, Transforms and operators for directional bioimage analysis: a survey, Focus on bio-image informatics , 69 (2016).

[37] R. Rezakhaniha, A. Agianniotis, J. T. C. Schrauwen, A. Griffa, D. Sage, C. v. Bouten, F. Van De Vosse, M. Unser, and N. Stergiopulos, Experimental investigation of collagen waviness and orientation in the arterial adventitia using confocal laser scanning microscopy, Biomechanics and modeling in mechanobiology **11**, 461 (2012).

[38] E. Fonck, G. G. Feigl, J. Fasel, D. Sage, M. Unser, D. A. Rüfenacht, and N. Stergiopulos, Effect of aging on elastin functionality in human cerebral arteries, Stroke **40**, 2552 (2009).

[39] S. Ishihara, P. Marcq, and K. Sugimura, From cells to tissue: A continuum model of epithelial mechanics, Physical Review E **96**, 022418 (2017).

[40] S. C. Takatori, W. Yan, and J. F. Brady, Swim pressure: stress generation in active matter, Physical review letters **113**, 028103 (2014).

[41] X. Yang, D. Bi, M. Czajkowski, M. Merkel, M. L. Manning, and M. C. Marchetti, Correlating cell shape and cellular stress in motile confluent tissues, Proceedings of the National Academy of Sciences **114**, 12663 (2017).